

Excitations of a supersolid annular stripe phase in a spin-orbital-angular-momentum-coupled spin-1 Bose-Einstein condensate

Paramjeet Banger,^{1,2,*} Rajat,^{1,†} and Sandeep Gautam^{1,‡}

¹*Department of Physics, Indian Institute of Technology Ropar, Rupnagar-140001, Punjab, India*

²*Department of Physics, Indian Institute of Science Education and Research Pune, Pune 411008, India*

We present a theoretical study of the collective excitations of the supersolid annular stripe phase of a spin-orbital-angular-momentum-coupled (SOAM-coupled) spin-1 Bose-Einstein condensate. The annular stripe phase simultaneously breaks two continuous symmetries, namely rotational and $U(1)$ gauge symmetry, and is more probable in the condensates with a larger orbital angular momentum transfer imparted by a pair of Laguerre-Gaussian beams than what has been considered in the recent experiments. Accordingly, we consider a SOAM-coupled spin-1 condensate with a $4\hbar$ orbital angular momentum transferred by the lasers. Depending on the values of the Raman coupling strength and quadratic Zeeman term, the condensate with realistic antiferromagnetic interactions supports three ground-state phases: the annular stripe, the vortex necklace, and the zero angular momentum phase. We numerically calculate the collective excitations of the condensate as a function of coupling and quadratic Zeeman field strengths for a fixed ratio of spin-dependent and spin-independent interaction strengths. At low Raman coupling strengths, we observe a direct transition from the zero angular momentum to the annular stripe phase, characterized by the softening of a double symmetric roton mode, which serves as a precursor to supersolidity.

I. INTRODUCTION

Unlike solids, where the electric field is crucial for generating spin-orbit (SO) coupling, ultracold neutral atoms do not exhibit SO coupling when exposed to an external electric field. Artificial gauge fields have emerged as a powerful tool which addresses this limitation, allowing the study of the Lorentz-like force on neutral atoms [1, 2]. The experimental realization of artificial gauge fields and the SO coupling that links spin with the linear momentum of neutral bosons [1–3] have opened up new unexplored avenues of research in this field [4, 5]. Synthetic SO coupling generated through Raman transitions has been successfully implemented in experimental setups for both bosonic [3, 6–8] and fermionic [9–11] atoms. This coupling in spinor Bose-Einstein condensates (BECs) gives rise to various ground-state phases, such as the supersolid stripe, the zero momentum, and the plane wave phases, which have been extensively investigated [3, 7, 8, 12–17]. In the context of these ground-state phases, elementary excitations can provide fundamental insights, particularly through softening of the roton mode as a precursor to crystallization of the stripe phase [18–21]. Elementary excitations have also been utilized to map the ground-state phase diagram in harmonically trapped SO-coupled BECs [6, 22–25].

Although SO coupling has been extensively studied in ultra-cold atoms, it is unlike the traditional SO coupling in atomic physics, which refers to the interaction between spin and orbital angular momentum. In this context, the spin-orbital-angular-momentum (SOAM) coupling, which couples the atoms' spin and the orbital angular momentum, was theoretically proposed [26–32] and later experimentally realized [33–36]. In these experiments, co-propagating Gaussian and

Laguerre-Gaussian (LG) laser beams along with a normally applied magnetic field have been used to couple two [33] or three spin states of ^{87}Rb [34, 35] from the $F = 1$ manifold to realize SOAM-coupled BECs and study their ground-state phases.

The primary ground-state phases of SOAM-coupled BECs can be broadly categorized as (a) the zero angular momentum (ZAM) phase, (b) the polarized phases, and (c) a variety of rotational symmetry-breaking phases [26–31, 37–42]. The zero angular momentum (ZAM) and the polarized phases are axisymmetric with well-defined angular momenta and have been observed experimentally [33–35]. Among the symmetry-breaking phases, an intriguing phase is the supersolid annular stripe (AS) phase, which corresponds to condensation in two single-particle states with opposite angular momenta. This phase breaks two continuous symmetries, namely $U(1)$ gauge and rotational symmetry, just like the supersolid stripe phase breaks the gauge and translational symmetries in the Raman-induced SO-coupled BECs [12, 13]. Due to the small contrast and spatial period of stripes, the AS phase has eluded the experimental detection. The effects of experimentally controllable parameters, such as angular momentum transferred to the atoms by the two LG beams, their waist sizes, the size of the BEC, and the interaction energy, on the feasibility of the experimental detection of the AS phase have been theoretically studied [39]. It has been shown that larger angular momentum transfer by the LG beams can improve the spatial contrast of the stripes [39]. In this context, the experimental realizations of SOAM-coupling have been with an angular momentum transfer of \hbar [33–35], while ground-state phases of the SOAM-coupled BECs have been examined with a larger momentum transferred by LG beams [29, 39, 41].

In addition to the exploration of the equilibrium ground-state phases, elementary excitations in the zero angular momentum and the polarized phases of a pseudospin-1/2 SOAM-coupled spinor BEC have been theoretically investigated [31, 38, 40, 43]. The low-lying modes in the excitation spectrum, such as dipole and breathing modes, of the half-skyrmion and

* paramjeet.banger@acads.iiserpune.ac.in

† rajat.19phz0009@iitrpr.ac.in

‡ sandeep@iitrpr.ac.in

vortex-antivortex phases have been studied in Refs. [31, 38]. For an SOAM-coupled spin-1 BEC with both antiferromagnetic and ferromagnetic, the low-lying excitation spectrum of the polar-core vortex (ZAM) and coreless vortex (polarized) phases have been examined [42]. Regarding this study, it has to be emphasized that due to a smaller angular momentum transfer of \hbar and the absence of the quadratic Zeeman field, the ground-state phase diagram did not have the AS phase. The quadratic Zeeman field serves as an additional experimental controllable parameter in a spin-1 BEC, unlike in a pseudospin-1/2 BEC, and permits an alternative route to drive the phase transitions [17, 20, 21, 25, 30]. In this work, we consider an SOAM-coupled spin-1 BEC with antiferromagnetic interactions and a higher angular momentum transfer of $4\hbar$ to allow for the emergence of the AS phase along with the ZAM and another symmetry-breaking vortex necklace (VN) phase [44, 45]. We examine the collective excitations of the system as a function of quadratic Zeeman field and Raman coupling strengths and illustrate the signature of crystallization via a softening of a characteristic symmetric double roton mode at the phase boundary.

The manuscript is organized as follows. In Sec. II, we discuss the ground-state solutions and energy spectrum of the non-interacting SOAM-coupled Hamiltonian for a spin-1 BEC. In Sec. III, we present the interacting mean-field model and calculate the phase diagram in Raman coupling versus quadratic Zeeman field strengths for an antiferromagnetic SOAM-coupled spin-1 BEC. In Sec. IV, we calculate collective excitations of the interacting SOAM-coupled spin-1 BEC and characterize a few low-lying modes. We provide a summary and conclusions of this study in Sec. V.

II. NON-INTERACTING HAMILTONIAN

We consider a non-interacting gas of SOAM-coupled spin-1 bosons in a quasi-2D harmonic trap. The (dimensionless) single-particle Hamiltonian of the system in the plane polar coordinates is [30, 34, 35]

$$H_0 = \left[-\frac{1}{2r} \frac{\partial}{\partial r} \left(r \frac{\partial}{\partial r} \right) + \frac{\hat{L}_z^2}{2} + \frac{r^2}{2} \right] + \Omega(r) [\cos(l\phi)S_x - \sin(l\phi)S_y] + qS_z^2, \quad (1)$$

where $\hat{L}_z = -i\partial/\partial\phi$ is the angular momentum operator, $\Omega(r) = \Omega_0 e^{\frac{1}{2}}(r/w)^l e^{-2r^2/w^2}$ is the spatially dependent Raman coupling strength [39] with Ω_0 and w as the Rabi frequency and beam waists of the two LG beams, respectively, q is the quadratic Zeeman term, and S_x, S_y and S_z are irreducible representations of the spin-1 angular momentum operators [34, 35]. Here, l is the orbital angular momentum transfer to the atoms by the two co-propagating LG beams of opposite orbital angular momenta. We consider a higher orbital angular momentum transfer of $l = 4$ with $w = 5$ to allow for the emergence of the distinctive annular stripe (AS) phase in contrast to what was considered in Refs. [30, 42]. By considering the unitary transforma-

tion of the Hamiltonian, with unitary operator $e^{-ilS_z\phi}$, the order parameter $\Psi = (\psi_{+1}, \psi_0, \psi_{-1})^T$ is transformed to $\Psi' = e^{-ilS_z\phi}\Psi = (e^{-il\phi}\psi_{+1}, \psi_0, e^{il\phi}\psi_{-1})^T$, where T denotes the transpose; the transformed Hamiltonian is

$$H'_0 = e^{-ilS_z\phi} H_0 e^{ilS_z\phi}, \\ = \left[-\frac{1}{2} \frac{\partial}{r \partial r} \left(r \frac{\partial}{\partial r} \right) + \frac{(\hat{L}_z + lS_z)^2}{2r^2} + \frac{r^2}{2} \right] \\ + \Omega(r)S_x + qS_z^2. \quad (2)$$

As H'_0 commutes with L_z , a complete set of energy eigenstates can be chosen, which are the eigenstates of L_z too. Accordingly, an arbitrary eigenstate of the single-particle Hamiltonian H'_0 can be defined as

$$\Psi'(r, \phi) = e^{il_z\phi} R(r), \quad (3)$$

where $R(r) = [\psi_{+1}(r), \psi_0(r), \psi_{-1}(r)]^T$ is the radial part of the order parameter. The orbital angular momentum $l_z = l_j \mp jl$ in the laboratory frame, where l_j is the angular momentum of the j th spin component [30, 46].

We solve the single-particle Schrödinger equation $H'_0\Psi'(r, \phi) = E\Psi'(r, \phi)$ to calculate the energy spectrum. The single-particle energy spectrum (equivalent to the lowest dispersion branch) for four pairs of (Ω_0, q) values is depicted in Fig. 1(a). The spectrum is characterized by two global

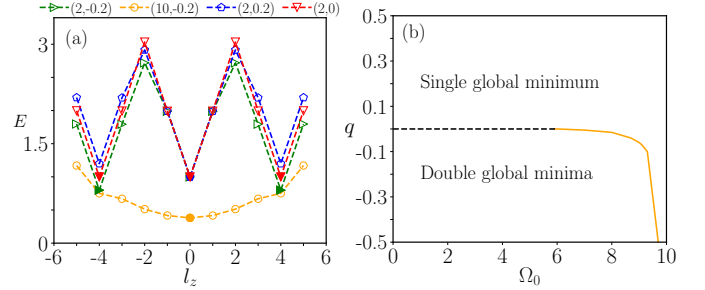


FIG. 1. (Color online) (a) The single-particle energy spectrum as a function of l_z for $(\Omega_0, q) = (2, -0.2), (2, 0), (2, +0.2)$ and $(10, -0.2)$. The spectrum has two degenerate global minima at $l_z = \pm 4$ for $(\Omega_0, q) = (2, -0.2)$, three degenerate global minima at $l_z = \pm 4, 0$ for $(\Omega_0, q) = (2, 0)$, and a single global minimum at $l_z = 0$ for $(\Omega_0, q) = (2, +0.2)$ and $(10, -0.2)$. (b) The single-particle phase diagram in the Ω_0, q plane. The single-particle spectrum is characterized by three degenerate global minima along the dashed part of the transition line.

minima for $\Omega = 2, q = -0.2$, a single global minimum for $\Omega = 2, q = 0.2$ and $\Omega = 10, q = -0.2$. The single-particle phase diagram shown in Fig. 1(b) has single and two global-minima regimes separated by a phase boundary across a portion of which the spectrum has three degenerate minima [30]. We also solve the single-particle Bogoliubov de-Gennes (BdG) equation to determine the single-particle excitation spectrum. For $q < q_c \leq 0$, where q_c represents the critical quadratic Zeeman field above which the energy spectrum has a single global minimum at $l_z = 0$, the lowest dispersion

branch exhibits two degenerate global minima for smaller values of Ω_0 . However, for larger values of Ω_0 , this branch has a single global minimum (see Fig. 2) in agreement with the single-particle energy spectrum.

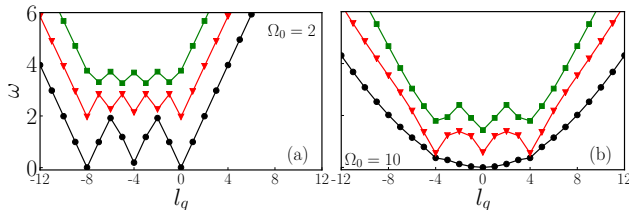


FIG. 2. (Color online) The single-particle excitation spectrum as a function of magnetic quantum number l_q associated with the angular momentum of the quasi-particle excitations: (a) $\Omega_0 = 2$, $q = -0.2$ and (b) $\Omega_0 = 10$, $q = -0.2$; the three lowest dispersion bands are shown. The lowest dispersion band has two global minima corresponding to two degenerate excitations with $l_q = -8$ and $l_q = 0$ for $\Omega_0 = 2$, whereas it has single minimum located at $l_q = 0$ for $\Omega_0 = 10$. Refer to Sec. IV for the methodology to calculate the excitation spectrum.

III. SOAM-COUPLED BEC WITH INTERACTIONS

At $T = 0$ K, a weakly-interacting SOAM-coupled quasi-2D spin-1 BEC is very well described by the Gross-Pitaevskii (GP) equation [30, 34, 35]

$$i \frac{\partial \Psi}{\partial t} = \left(H_0 + \frac{c_0 \rho}{2} + \frac{c_2 \mathbf{F} \cdot \mathbf{S}}{2} \right) \Psi, \quad (4)$$

where

$$\rho = \Psi^\dagger \Psi = \sum_{j=\pm 1,0} |\psi_j(r, \phi)|^2, \text{ and } \mathbf{F} = \Psi^\dagger \mathbf{S} \Psi$$

with \mathbf{S} denoting the vector of spin-1 matrices. In Eq. (4), c_0 and c_2 are interaction strengths for the quasi-2D spin-1 BEC defined as

$$c_0 = \sqrt{8\pi\alpha} \frac{N(a_0 + 2a_2)}{3a_{\text{osc}}}, \quad c_2 = \sqrt{8\pi\alpha} \frac{N(a_2 - a_0)}{3a_{\text{osc}}}, \quad (5)$$

where $\alpha = \omega_z/\omega_r$ is the ratio of the axial to the radial frequency, N is the total number of atoms in the condensate, $a_{\text{osc}} = \sqrt{\hbar/m\omega_r}$, and a_0 and a_2 are the s -wave scattering lengths in total spin equal to 0 and 2 channels, respectively. The interactions can lead to ground-state phases like the AS and the VN phases, which spontaneously break the rotational symmetry of the system. To realize the AS phase, in particular, we consider a ^{23}Na BEC with antiferromagnetic interactions ($c_2 < 0$) in this work. We consider 10^5 atoms of ^{23}Na confined in an axisymmetric harmonic trap with $\omega_r = 2\pi \times 37$ Hz and $\omega_z = 2\pi \times 1000$ Hz, which tightly confines the system along the z -axis. The doublet of s -wave scattering lengths are $(a_0, a_2) = (50a_B, 55.01a_B)$, where a_B as the Bohr radius [47], and the corresponding interaction parameters are

$c_0 = 42.57$, $c_2 = 1.33$. We solve the time-independent version of the GP equation (4) using imaginary-time propagation implemented via a time-splitting Fourier pseudospectral method [48]. The imaginary-time propagation, initiated with a suitable initial guess solution, facilitates a quick convergence towards the ground state. Inspired by the eigenfunctions of the single-particle Hamiltonian, we consider initial guess solutions of form $\Psi \sim e^{-(x^2+y^2)/2} \times [(x+iy)^{k+4}, -\sqrt{2}(x+iy)^k, (x+iy)^{k-4}]^T$, where k is an integer; additionally, we consider random guess solutions generated using a Gaussian random number generator.

Ground-state phases: The system supports three ground-state phases in the Ω_0 - q plane for $c_0 = 42.57$ and $c_2 = 1.33$, namely the AS, the VN, and the ZAM phase. The representative density and phase profiles of the phases are shown in Fig. 3. The AS and the VN phases break the rotational symmetry [see Figs. 3(a) and (b)] with $\int \Psi^\dagger(x, y) \hat{L}_z \Psi(x, y) dx dy = \langle \hat{L}_z \rangle \neq 0$, whereas the ZAM phase is circularly symmetric with $\langle \hat{L}_z \rangle = 0$ or zero-angular momentum per particle [see Figs. 3(c) and (f)]. The AS phase has a stripe pattern along the azimuthal direction in the density profile, and the VN phase has four ± 1 charged phase singularities in $j = \pm 1$ component arranged along a circle. The ZAM phase is characterized by centrally located $4j$ phase singularity in the j th spin component. The ZAM phase, therefore, corresponds to the condensation occurring in a single particle state with $l_z = 0$, whereas the AS phase corresponds to the condensation in a superposition of two single-particle states with $l_z = +4$ and -4 . The three phases have distinctive topological spin-texture $\mathbf{F} = (F_x, F_y, F_z)$ as shown in Fig. 4. The AS phase has $F_z = 0$ with nonzero $\mathbf{F} \approx F_x \hat{x}$ which is oppositely aligned in adjacent lobes of the texture and [see Fig. 4(a)]. The VN and the ZAM phases have qualitatively similar projections of the spin textures on the x - y plane, i.e., \mathbf{F}_\perp . However, F_z is nonzero for the VN phase with the opposite signs in adjacent lobes of the texture and is zero for the ZAM phase and [see Figs. 4 (b) and (c)].

The ground-state phase diagram in the Ω_0 - q plane for the BEC with $c_0 = 42.57$ and $c_2 = 1.33$ is shown in Fig. 5. For $q > 0$, the ground state phase is the circularly symmetric ZAM phase with $l_z = 0$. For smaller Raman coupling strengths $\Omega < 3.5$, as q decreases (made more negative), there is a direct phase transition from the ZAM to the AS phase, whereas for $\Omega > 3.5$, the ZAM phase first transitions to the VN phase and then to the AS phase. The three phases coexist at the tricritical point. In the following section, we examine the collective excitations for (a) as a function of q for $\Omega_0 = 2$, (b) as a function of q for $\Omega_0 = 5$, and (c) as a function of Ω_0 for $q = -0.2$. The variation of energy and its first-order derivative for these three cases are shown in Figs. 6(a)-6(c). The direct phase transition from the ZAM phase to the AS phase is a first-order phase transition [see Fig. 6(a)], whereas, in the presence of the intervening VN phase, the AS-VN and the VN-ZAM phase transitions are continuous [see Figs. 6(b) and 6(c)].

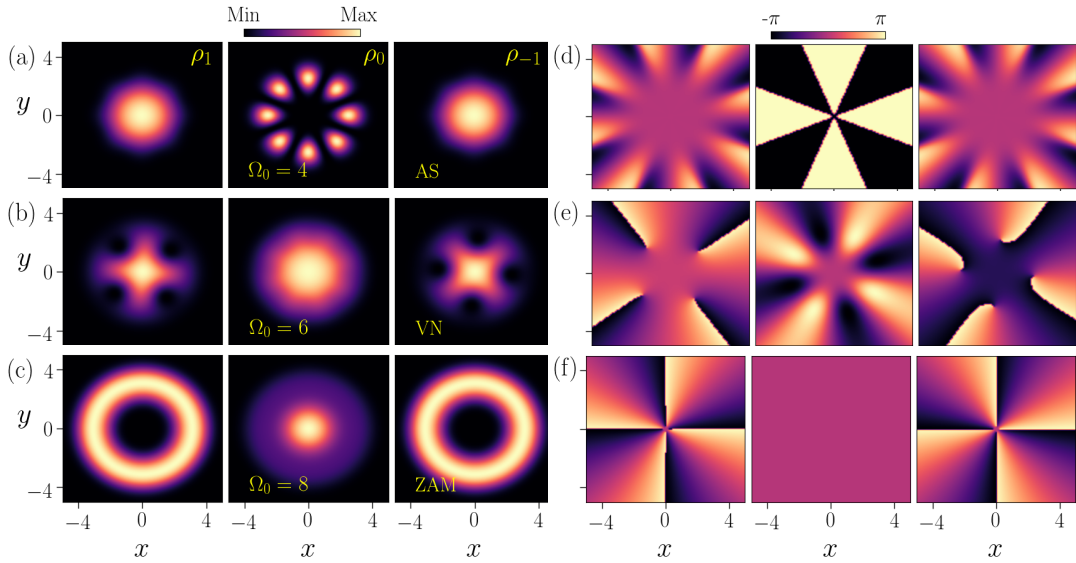


FIG. 3. (Color online) The density and the phase structures of the ground state phases of the SOAM-coupled spin-1 BEC with $c_0 = 42.57$, $c_2 = 1.33$ and $q = -0.2$. The component densities in (a) the annular stripe (AS) phase with $\Omega_0 = 4$, (b) the vortex necklace (VN) phase with $\Omega_0 = 6$, and (c) the zero angular-momentum (ZAM) phase with $\Omega_0 = 8$. The phase profiles corresponding to (a), (b), and (c) are displayed in (d), (e), and (f), respectively.

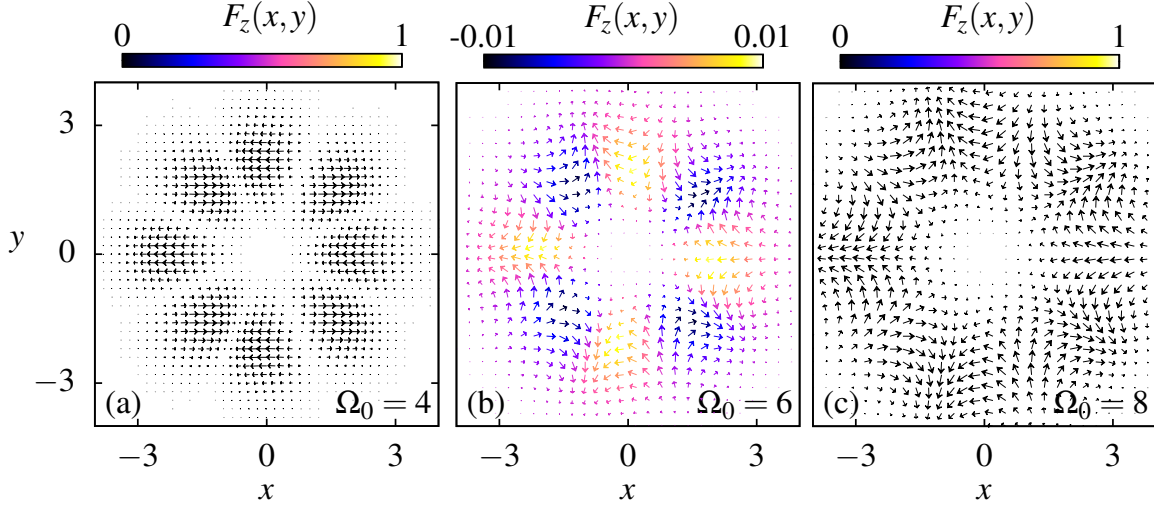


FIG. 4. (Color online) The spin-texture of SOAM-coupled spin-1 BEC with $c_0 = 42.57$, $c_2 = 1.33$ and $q = -0.2$: (a) $\Omega_0 = 4$, (b) $\Omega_0 = 6$, and (c) $\Omega_0 = 8$. The arrows show the projection of $\mathbf{F}(x, y)$ on the x - y plane, and the color indicates its component along the z axis.

IV. COLLECTIVE EXCITATIONS

We use the Bogoliubov approach to calculate the collective excitation spectrum of the SOAM-coupled BEC, where we first linearize the GP equation (4) by perturbing the order parameter as

$$\Psi(x, y, t) = e^{-i\mu t} [\Psi_{\text{eq}}(x, y) + \delta\Psi(x, y, t)], \quad (6)$$

where $\Psi_{\text{eq}}(x, y) = [\psi_{+1}(x, y), \psi_0(x, y), \psi_{-1}(x, y)]^T$ is the ground-state order parameter, and μ is the chemical potential. We substitute the fluctuation $\delta\Psi(x, y, t) = \mathbf{u}_\lambda(x, y)e^{-i\omega_\lambda t} -$

$\mathbf{v}_\lambda^*(x, y)e^{i\omega_\lambda t}$ in the linearized GP equation, where $\mathbf{u}_\lambda(x, y)$ and $\mathbf{v}_\lambda(x, y)$ are Bogoliubov quasi-particle amplitudes and ω_λ is the excitation frequency with λ as the frequency index. This leads to the following set of coupled Bogoliubov-de Gennes (BdG) equations

$$\begin{pmatrix} P_1 & P_2 \\ -P_2^* & -P_1^* \end{pmatrix} \begin{pmatrix} \mathbf{u}_\lambda \\ \mathbf{v}_\lambda \end{pmatrix} = \omega_\lambda \begin{pmatrix} \mathbf{u}_\lambda \\ \mathbf{v}_\lambda \end{pmatrix}, \quad (7)$$

where $\mathbf{u}_\lambda = (u_{+1,\lambda}, u_{0,\lambda}, u_{-1,\lambda})^T$, $\mathbf{v}_\lambda = (v_{+1,\lambda}, v_{0,\lambda}, v_{-1,\lambda})^T$, and P_1 and P_2 are defined in the Appendix. We use a basis expansion method with a truncated set of eigenfunctions of a two-dimensional harmonic oscilla-

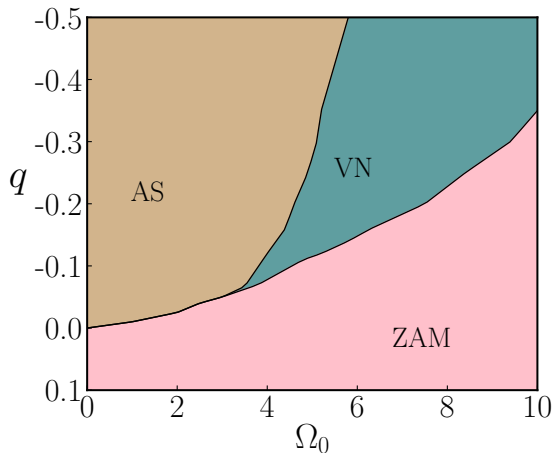


FIG. 5. (Color online) The phase diagram of an SOAM-coupled spin-1 BEC in the $\Omega_0 - q$ plane with $c_0 = 42.57$ and $c_2 = 1.33$. The three phases coexist at the tricritical point ($\Omega_0 = 3.5$, $q = -0.06$).

tor serving as the requisite basis to solve the BdG equation as discussed in the Appendix. The excitations can also be characterized by the magnetic quantum number l_q for the circular-symmetric ZAM phase. In this case, the GP equation can be linearized using the perturbed order parameter

$$\Psi(r, \phi, t) = e^{-i\mu t + i(l_z + S_z)\phi} [\Psi_{\text{eq}}(r) + \delta\Psi(r, t)e^{il_q\phi}],$$

which, followed by the Bogoliubov transformation, leads to a circularly symmetric set of BdG equation [42].

In Fig. 7(a), we show the excitation spectrum of the BEC with $c_0 = 42.57$ and $c_2 = 1.33$ as a function of quadratic Zeeman field q for Raman coupling strength $\Omega_0 = 2$. In this case, as q is decreased, it leads to a direct phase transition from the ZAM phase to the AS phase, as discussed in Sec. III. With a decrease in q , a double symmetric roton mode [20, 21, 25] corresponding to $l_q = \pm 4$ softens and becomes zero at (critical) Zeeman field $q \approx -0.016$ as shown in Fig. 7(a). At this point, a transition occurs from the ZAM phase to the AS phase. This double symmetric roton structure is clearly visible in Fig. 7(b), where we plot the excitation spectrum as a function of the magnetic quantum number l_q for $q = 0.2$ and $q = -0.016$. For the circularly symmetric ZAM phase, the modes with $l_q \neq 0$ are doubly degenerate, whereas those with $l_q = 0$ are non-degenerate. This is a consequence of the invariance of the BdG equation, under the transformation $l_q \rightarrow -l_q$ with a simultaneous interchange of $+1$ and -1 spin states for $l_z = 0$ [42]. Some low-lying modes can be excited and identified by adding a suitable time-independent perturbation proportional to an observable \hat{O} to the Hamiltonian at $t = 0$ and then examining the time evolution $\langle \hat{O} \rangle = \int \Psi^\dagger(x, y, t) \hat{O} \Psi(x, y, t) dr$, where $\Psi(x, y, t = 0)$ is the ground-state order parameter of the unperturbed Hamiltonian. The \hat{O} can be chosen as x or y for the dipole, xS_z or yS_z for the spin-dipole [23], x^2 or y^2 for the breathing and x^2S_z or y^2S_z for the spin-breathing mode. The $\langle \hat{O} \rangle$ oscillates at a dominant frequency, which

can be extracted from its Fourier transform [42, 49]. The density and spin dipole modes correspond, respectively, to the oscillations of the center of masses of $\rho(x, y)$ and $F_z(x, y)$, while the breathing modes refer to the oscillations of the root-mean-square sizes of these distributions. The method has been used experimentally to excite the density [50] and spin dipole modes [51] by modulating the harmonic trapping potential. The dipole and the breathing modes change discontinuously across the ZAM-AS phase boundary [see Fig. 7(a)], highlighting the first-order nature of the transition in agreement with Fig. 6(a). The AS phase breaks two continuous symmetries, gauge and rotational symmetries, resulting in two zero-energy Goldstone modes in the excitation spectrum, whereas for the ZAM phase, we observe a single Goldstone mode due to the breaking of $U(1)$ gauge symmetry. This first-order phase transition at low Ω is qualitatively similar to one studied in an SO-coupled spin-1 BEC with antiferromagnetic interactions [25]. In both systems, the double symmetric roton mode, along with other low-lying modes, softens with a decrease in quadratic Zeeman field strength [25], with vanishing roton gaps marking the transition to the supersolid annular or rectilinear stripes.

Next, we fix Ω_0 at 5 and examine the excitation spectrum as a function of q . In this case, with a decrease in q from 0 to -0.5, there is a phase transition from the VN to the ZAM phase and then a transition from the VN to the AS phase [see Fig. 5] The excitation spectrum is shown in Fig. 8. Notably, both the transitions, from the AS to the VN and from the VN to the ZAM phase, are second-order transitions as evidenced by no discernible discontinuities across the critical points in Fig. 8 and in agreement with the results in Fig. 6(b). The dispersion (ω versus l_q) for the ZAM phase again has a symmetric double-roton structure (not shown here), with roton gaps at $l_q = \pm 4$ closing at the ZAM-VN phase boundary. Like the supersolid AS, the VN phase breaks the two continuous symmetries, resulting in two zero-energy Goldstone modes. In the VN phase, $\langle \hat{O} \rangle$ does not oscillate at a single dominant frequency for any of the \hat{O} mentioned earlier, leading to the multiple peaks in the Fourier transform of $\langle \hat{O} \rangle$. Due to this, we can not unambiguously identify dipole and breathing modes for this phase.

Lastly, we keep the quadratic Zeeman field $q = -0.2$ fixed and vary the Raman coupling strength Ω_0 from 0 to 10. As the Raman coupling strength increases, a second-order transition from the AS to the VN phase is observed above a critical coupling $\Omega_0 \approx 4.6$. As we further increase the Raman coupling strength, the system undergoes another continuous phase transition from the VN to the ZAM phase above $\Omega_0 \approx 7.4$. In the AS phase, the low-lying modes, namely the density dipole, density breathing, spin-dipole, and spin-breathing modes, decrease with increasing Ω_0 . Similarly, in the ZAM phase, two density modes decrease with increasing Ω_0 [see Fig. 9].

V. SUMMARY AND CONCLUSIONS

We studied the ground-state phases and the low-lying collective excitations of a quasi-2D SOAM-coupled spin-1 BEC with antiferromagnetic interactions. We used the SOAM

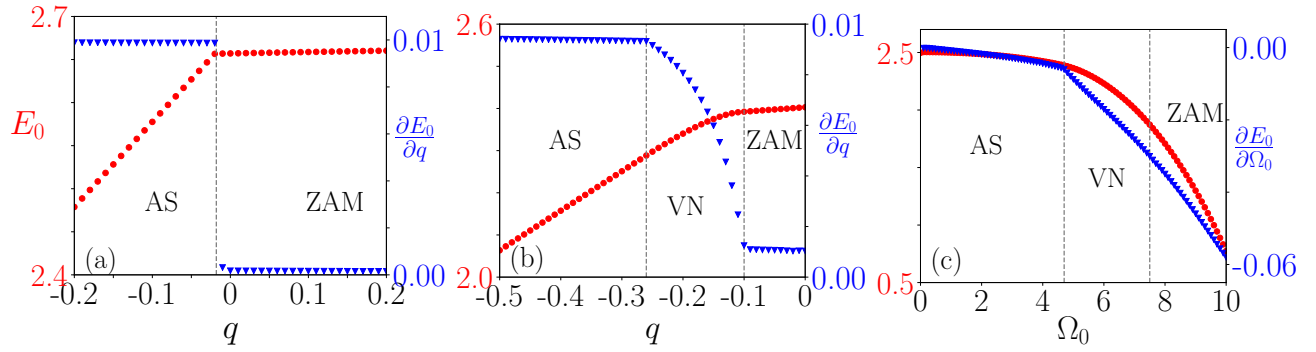


FIG. 6. The ground state energy E_0 and $\partial E_0/\partial q$ as a function of q for the BEC with $c_0 = 42.57$, $c_2 = 1.33$: (a) $\Omega_0 = 2$ and (b) $\Omega_0 = 5$. (c) the ground state energy E_0 and $\partial E_0/\partial \Omega_0$ as a function of Ω_0 for the BEC with the same interaction parameters. The dashed vertical lines correspond to the transition points. The first-order derivative of energy changes discontinuously across the AS-ZAM transition point in (a), whereas it is continuous at the AS-VN and the VN-ZAM transition points in (b) and (c).

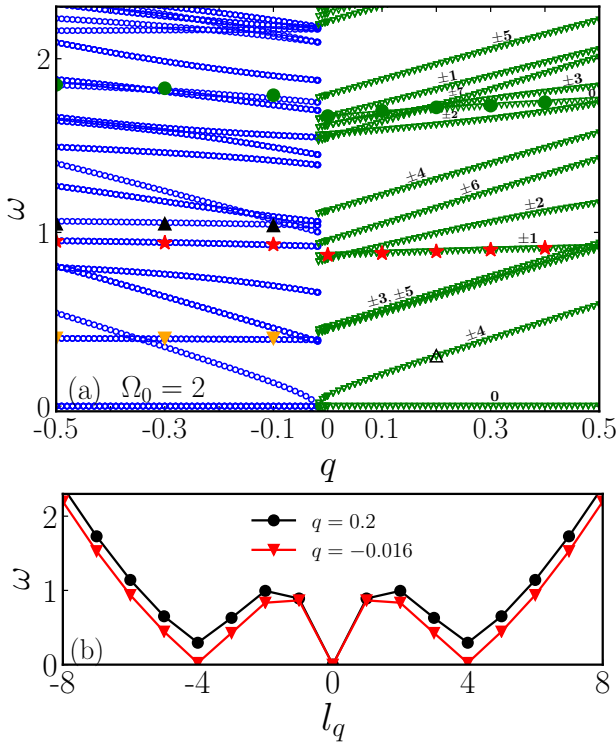


FIG. 7. (a) The low-lying excitation spectrum of the SOAM-coupled spin-1 BEC with $c_0 = 42.57$, $c_2 = 1.33$, and $\Omega_0 = 2$ as a function of q . For $q \gtrsim -0.017$, there is a phase transition from the AS to the circularly symmetric $l_z = 0$ (ZAM) phases. In both the AS and the ZAM phases, dipole and breathing modes are marked by red stars and green circles. Spin-dipole and spin-breathing modes are marked by orange lower and black upper triangles in the AS phase. For the circularly-symmetric ZAM phase, all the excitations are labelled with their respective magnetic quantum number l_q , which is not a good quantum number to characterize the excitations of the AS phase; the labels have been placed above to their corresponding excitation frequencies. (b) Illustrates the excitation spectrum as a function of the magnetic quantum number l_q in the ZAM phase, where the roton minima occur at $l_q = \pm 4$.

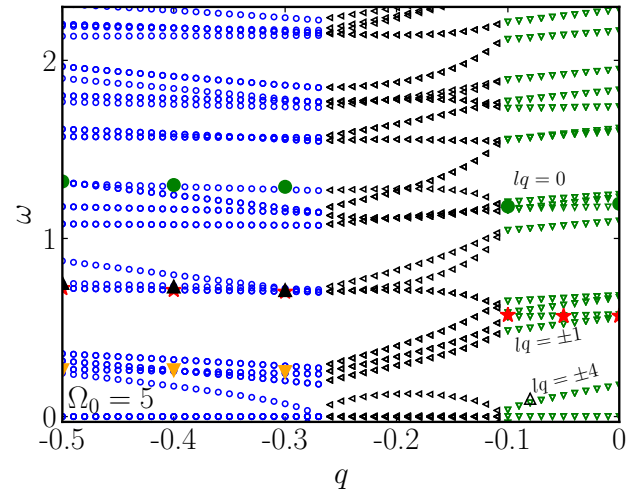


FIG. 8. (Color online) The excitation spectrum of the SOAM-coupled spin-1 BEC with $c_0 = 42.57$, $c_2 = 1.33$, and $\Omega_0 = 5$ as a function of q . The blue “circles”, black “triangles” and green “downtriangles” correspond, respectively, to the annular stripe (AS), the vortex necklace (VN), and the zero angular momentum (ZAM) phases. In the AS phase, dipole, breathing, spin-dipole, and spin-breathing modes are marked by red stars, green circles, orange lower and black upper triangles, respectively. In the ZAM phase, dipole ($l_q = \pm 1$) and breathing modes ($l_q = 0$) are marked by red stars and green circles. For $q \gtrsim -0.26$, there is a phase transition from the AS to the VN, and for $q \gtrsim -0.1$, a phase transition from the VN to the ZAM phase. The excitation mode with $l_q = \pm 4$ in the ZAM phase is the double roton mode.

coupling corresponding to an angular momentum transfer of $l = 4\hbar$ to the atoms, which allows the annular stripe phase as one of the ground state phases alongside a circularly symmetric (zero angular momentum) phase and another symmetry-breaking vortex necklace phase for c_2/c_0 corresponding to ^{23}Na . We calculated the phase diagram in the plane of Raman coupling strength Ω_0 versus the quadratic Zeeman field strength q for both the non-interacting and interacting condensates. Using the Bogoliubov approach, we numerically calculated the excitation spectrum of the system with fixed in-

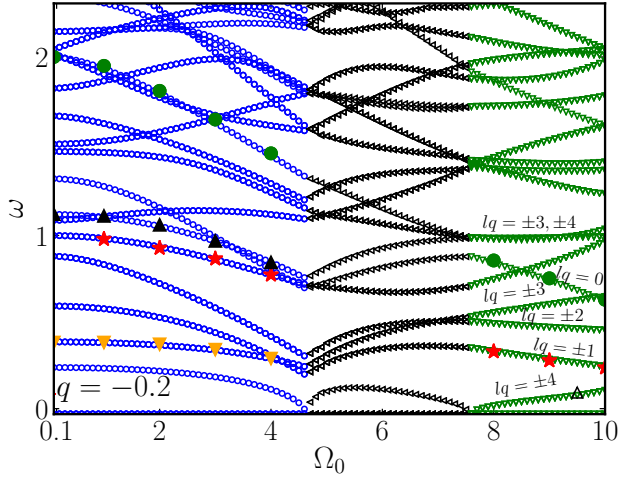


FIG. 9. (Color online) The excitation spectrum of the SOAM-coupled spin-1 BEC with $c_0 = 42.57$, $c_2 = 1.33$, and $q = -0.2$ as a function of Ω_0 . The blue “circles”, black “triangles” and green “downtriangles” correspond, respectively, to annular stripe (AS), vortex necklace (VN), and zero angular momentum (ZAM) phases. In the AS phase, dipole, breathing, spin-dipole, and spin-breathing modes are marked by red stars, green circles, orange lower and black upper triangles, respectively. In the ZAM phase, dipole ($l_q = \pm 1$) and breathing ($l_q = 0$) are marked by red stars and green circles. For $\Omega_0 \gtrsim 4.6$, there is a phase transition from the AS to the VN phase, and at $\Omega_0 \gtrsim 7.4$, a phase transition from VN to ZAM phases. The excitation mode with $l_q = \pm 4$ in the ZAM phase is the double roton mode and softens at the ZAM-VN transition point.

interaction strengths in three scenarios: (a) as a function of q for a small fixed value of Ω_0 , (b) as a function of q for Ω_0 fixed to a relatively higher value, and (c) as a function of Ω_0 for a fixed q . For (a), the excitation spectrum reveals a first-order phase transition from the ZAM to the AS phase directly which is accompanied by the closing of double symmetric roton gaps, a signature of crystallization or supersolidity. This is similar to the zero momentum to the supersolid stripe phase transition in a SO-coupled BEC. For (b) and (c), the continuous ZAM to the VN phase transition is also characterized by the closing double symmetric roton gaps. We identified a few low-lying collective modes, such as dipole and breathing modes, in both the AS and VN phases.

ACKNOWLEDGMENTS

S.G. acknowledges support from the Science and Engineering Research Board, Department of Science and Technology, Government of India through Project No. CRG/2021/002597.

APPENDIX: A BASIS SET EXPANSION METHOD TO SOLVE THE BDG EQUATIONS

Here, we discuss the details of the numerical method to solve the BdG equation (7), where P_1 and P_2 are defined as

$$P_1 = \begin{bmatrix} \mathcal{H} - \mu + c_0\rho_{+1} + c_2(2\rho_{+1} + \rho_0 - \rho_{-1}) & (c_0 + c_2)\psi_0^*\psi_{+1} + 2c_2\psi_{-1}^*\psi_0 + \mathcal{H}_\Omega & (c_0 - c_2)(\psi_{-1}\psi_{+1}^*) \\ (c_0 + c_2)\psi_0\psi_{+1}^* + 2c_2\psi_{-1}\psi_0^* + \mathcal{H}_\Omega^* & \mathcal{H} - \mu + c_0\rho_0 + c_2(\rho_{+1} + \rho_{-1}) & (c_0 + c_2)\psi_0\psi_{-1}^* + 2c_2\psi_{+1}\psi_0^* + \mathcal{H}_\Omega \\ (c_0 - c_2)(\psi_{+1}^*\psi_{-1}) & (c_0 + c_2)\psi_0^*\psi_{-1} + 2c_2\psi_{+1}^*\psi_0 + \mathcal{H}_\Omega^* & \mathcal{H} - \mu + c_0\rho_{-1} + c_2(\rho_0 - \rho_{+1} + 2\rho_{-1}) \end{bmatrix},$$

$$P_2 = \begin{bmatrix} (c_0 + c_2)\psi_{+1}^2 & (c_0 + c_2)\psi_0\psi_{+1} & (c_0 - c_2)\psi_{-1}\psi_{+1} + c_2\psi_0^2 \\ (c_0 + c_2)\psi_{+1}\psi_0 & c_0\psi_0^2 + 2c_2\psi_{+1}\psi_{-1} & (c_0 + c_2)\psi_{-1}\psi_0 \\ (c_0 - c_2)\psi_{+1}\psi_{-1} + c_2\psi_0^2 & (c_0 + c_2)\psi_0\psi_{-1} & (c_0 + c_2)\psi_{-1}^2 \end{bmatrix},$$

with

$$\mathcal{H} = \left(-\frac{1}{2}\partial_x^2 - \frac{1}{2}\partial_y^2 + V(x, y) + c_0\rho \right), \text{ and}$$

$$\mathcal{H}_\Omega = \frac{\Omega(r)}{\sqrt{2}} e^{il\phi}.$$

To solve the BdG equation (7), we express BdG amplitudes $u_{j,\lambda}(x, y)$ and $v_{j,\lambda}(x, y)$ as a linear combination of N_b low-lying eigenstates of two-dimensional harmonic oscillator [52]

$$u_{j,\lambda}(x, y) = \sum_{n=0}^{N_b-1} c_{j,n+1}^\lambda \varphi_n(x, y), \quad (8)$$

$$v_{j,\lambda}(x, y) = \sum_{n=0}^{N_b-1} d_{j,n+1}^\lambda \varphi_n(x, y), \quad (9)$$

where $j = +1, 0, -1$ and $c_{j,n+1}^\lambda$ and $d_{j,n+1}^\lambda$ are the constant coefficients. The n th harmonic oscillator basis state is

$$\varphi_n(x, y) = \xi_{n_x}(x)\xi_{n_y}(y), \quad (10)$$

where $\xi_{n_x}(x)[\xi_{n_y}(y)]$ is a normalized eigen state of one-dimensional harmonic oscillator with $n_x = 0, 1, \dots, n_x^{\max}$ ($n_y = 0, 1, \dots, n_y^{\max}$), and $n = n_y(n_x^{\max} + 1) + n_x$ for $n_y^{\max} \geq n_x^{\max}$. In this work, with an isotropic confinement along the $x - y$ plane, we consider $n_x^{\max} = n_y^{\max}$. Projecting the six-coupled BdG equations on $N_b = (n_x^{\max} + 1)^2$ harmonic oscillator states, we get $6N_b$ equations, which can be

written in the 6×6 matrix form as

$$\begin{bmatrix} \mathcal{M}_{11} & \mathcal{M}_{12} & \mathcal{M}_{13} & \mathcal{M}_{14} & \mathcal{M}_{15} & \mathcal{M}_{16} \\ \mathcal{M}_{21} & \mathcal{M}_{22} & \mathcal{M}_{23} & \mathcal{M}_{24} & \mathcal{M}_{25} & \mathcal{M}_{26} \\ \mathcal{M}_{31} & \mathcal{M}_{32} & \mathcal{M}_{33} & \mathcal{M}_{34} & \mathcal{M}_{35} & \mathcal{M}_{36} \\ \mathcal{M}_{41} & \mathcal{M}_{42} & \mathcal{M}_{43} & \mathcal{M}_{44} & \mathcal{M}_{45} & \mathcal{M}_{46} \\ \mathcal{M}_{51} & \mathcal{M}_{52} & \mathcal{M}_{53} & \mathcal{M}_{54} & \mathcal{M}_{55} & \mathcal{M}_{56} \\ \mathcal{M}_{61} & \mathcal{M}_{62} & \mathcal{M}_{63} & \mathcal{M}_{64} & \mathcal{M}_{65} & \mathcal{M}_{66} \end{bmatrix} \begin{bmatrix} \mathbf{c}_{+1}^\lambda \\ \mathbf{c}_0^\lambda \\ \mathbf{c}_{-1}^\lambda \\ \mathbf{d}_{+1}^\lambda \\ \mathbf{d}_0^\lambda \\ \mathbf{d}_{-1}^\lambda \end{bmatrix} = \omega_\lambda \begin{bmatrix} \mathbf{c}_{+1}^\lambda \\ \mathbf{c}_0^\lambda \\ \mathbf{c}_{-1}^\lambda \\ \mathbf{d}_{+1}^\lambda \\ \mathbf{d}_0^\lambda \\ \mathbf{d}_{-1}^\lambda \end{bmatrix}. \quad (11)$$

In Eq. (11), \mathbf{c}_j^λ and \mathbf{d}_j^λ are $N_b \times 1$ column vectors defined as

$$\mathbf{c}_j^\lambda = (c_{j,1}^\lambda, c_{j,2}^\lambda, \dots, c_{j,N_b}^\lambda)^T, \quad (12)$$

$$\mathbf{d}_j^\lambda = (d_{j,1}^\lambda, d_{j,2}^\lambda, \dots, d_{j,N_b}^\lambda)^T, \quad (13)$$

and the six elements of the block matrix \mathcal{M} on the left hand side are $N_b \times N_b$ matrices with their kl th element defined as follows

$$\mathcal{M}_{11}^{kl} = \iint \varphi_p(x, y) \left[-\frac{1}{2}\partial_x^2 - \frac{1}{2}\partial_y^2 - \mu + V(x, y) + c_0\rho + c_0\rho_{+1} + c_2(2\rho_{+1} + \rho_0 - \rho_{-1}) \right] \varphi_q(x, y) dx dy,$$

$$\mathcal{M}_{12}^{kl} = \iint \varphi_p(x, y) \left[(c_0 + c_2)\psi_0^*\psi_{+1} + 2c_2\psi_{-1}^*\psi_0 + h_{cc} \right] \varphi_q(x, y) dx dy,$$

$$\mathcal{M}_{13}^{kl} = \iint \varphi_p(x, y)(c_0 - c_2)(\psi_{-1}\psi_{+1}^*)\varphi_q(x, y) dx dy, \quad \mathcal{M}_{14}^{kl} = \iint \varphi_p(x, y)(c_0 + c_2)\psi_{+1}^2\varphi_q(x, y) dx dy,$$

$$\mathcal{M}_{15}^{kl} = \iint \varphi_p(x, y)(c_0 + c_2)\psi_0\psi_{+1}\varphi_q(x, y) dx dy, \quad \mathcal{M}_{16}^{kl} = \iint \varphi_p(x, y) \left[(c_0 - c_2)\psi_{-1}\psi_{+1} + c_2\psi_0^2 \right] \varphi_q(x, y) dx dy,$$

$$\mathcal{M}_{21}^{kl} = \iint \varphi_p(x, y) \left[(c_0 + c_2)\psi_0\psi_{+1}^* + 2c_2\psi_{-1}\psi_0^* + h_{cc}^* \right] \varphi_q(x, y) dx dy,$$

$$\mathcal{M}_{22}^{kl} = \iint \varphi_p(x, y) \left[-\frac{1}{2}\partial_x^2 - \frac{1}{2}\partial_y^2 - \mu + V(x, y) + c_0\rho + c_2(\rho_{+1} + \rho_{-1}) \right] \varphi_q(x, y) dx dy,$$

$$\mathcal{M}_{23}^{kl} = \iint \varphi_p(x, y) \left[(c_0 + c_2)\psi_{-1}^*\psi_0 + 2c_2\psi_0^*\psi_{+1} + h_{cc} \right] \varphi_q(x, y) dx dy,$$

$$\mathcal{M}_{24}^{kl} = \iint \varphi_p(x, y)(c_0 + c_2)(\psi_{+1}\psi_0)\varphi_q(x, y) dx dy,$$

$$\mathcal{M}_{25}^{kl} = \iint \varphi_p(x, y) \left[c_0\psi_0^2 + 2c_2\psi_{-1}\psi_{+1} \right] \varphi_q(x, y) dx dy,$$

$$\mathcal{M}_{26}^{kl} = \iint \varphi_p(x, y)(c_0 + c_2)\psi_{-1}\psi_0\varphi_q(x, y) dx dy,$$

$$\mathcal{M}_{31}^{kl} = -\iint \varphi_p(x, y)(c_0 - c_2)\psi_{+1}^*\psi_{-1}\varphi_q(x, y) dx dy,$$

$$\mathcal{M}_{32}^{kl} = -\iint \varphi_p(x, y) \left[(c_0 + c_2)\psi_0^*\psi_{-1} + 2c_2\psi_{+1}^*\psi_0 + h_{cc}^* \right] \varphi_q(x, y) dx dy,$$

$$\mathcal{M}_{33}^{kl} = -\iint \varphi_p(x, y) \left[-\frac{1}{2}\partial_x^2 - \frac{1}{2}\partial_y^2 - \mu + V(x, y) + c_0\rho + c_0\rho_{-1} + c_2(\rho_0 - \rho_{+1} + 2\rho_{-1}) \right] \varphi_q(x, y) dx dy,$$

$$\mathcal{M}_{34}^{kl} = -\iint \varphi_p(x, y) \left[(c_0 - c_2)\psi_{+1}\psi_{-1} + c_2\psi_0^2 \right] \varphi_q(x, y) dx dy,$$

$$\mathcal{M}_{35}^{kl} = -\iint \varphi_p(x, y) \left[(c_0 + c_2)\psi_0\psi_{-1} \right] \varphi_q(x, y) dx dy,$$

$$\mathcal{M}_{36}^{kl} = -\iint \varphi_p(x, y) \left[(c_0 + c_2)\psi_{-1}^2 \right] \varphi_q(x, y) dx dy,$$

$$\begin{aligned} \mathcal{M}_{41}^{kl} &= -(\mathcal{M}_{14}^{kl})^*, & \mathcal{M}_{42}^{kl} &= -(\mathcal{M}_{15}^{kl})^*, & \mathcal{M}_{43}^{kl} &= -(\mathcal{M}_{16}^{kl})^*, & \mathcal{M}_{44}^{kl} &= -(\mathcal{M}_{11}^{kl})^*, & \mathcal{M}_{45}^{kl} &= -(\mathcal{M}_{12}^{kl})^*, & \mathcal{M}_{46}^{kl} &= -(\mathcal{M}_{13}^{kl})^*, \\ \mathcal{M}_{51}^{kl} &= -(\mathcal{M}_{24}^{kl})^*, & \mathcal{M}_{52}^{kl} &= -(\mathcal{M}_{25}^{kl})^*, & \mathcal{M}_{53}^{kl} &= -(\mathcal{M}_{26}^{kl})^*, & \mathcal{M}_{54}^{kl} &= -(\mathcal{M}_{21}^{kl})^*, & \mathcal{M}_{55}^{kl} &= -(\mathcal{M}_{22}^{kl})^*, & \mathcal{M}_{56}^{kl} &= -(\mathcal{M}_{23}^{kl})^*, \\ \mathcal{M}_{61}^{kl} &= -(\mathcal{M}_{34}^{kl})^*, & \mathcal{M}_{62}^{kl} &= -(\mathcal{M}_{35}^{kl})^*, & \mathcal{M}_{63}^{kl} &= -(\mathcal{M}_{36}^{kl})^*, & \mathcal{M}_{64}^{kl} &= -(\mathcal{M}_{31}^{kl})^*, & \mathcal{M}_{65}^{kl} &= -(\mathcal{M}_{32}^{kl})^*, & \mathcal{M}_{66}^{kl} &= -(\mathcal{M}_{33}^{kl})^*, \end{aligned}$$

where p and q can have values $0, 1, 2, \dots, N_b - 1$, $k = p + 1$, and $l = q + 1$. We opt for a sparse matrix representation to

store the BdG matrix and employ the ARPACK library [53] for diagonalization. LAPACK subroutines [54] can also efficiently handle the diagonalization of the matrix for small N_b .

[1] Y.-J. Lin, R. L. Compton, K. Jiménez-García, J. V. Porto, and I. B. Spielman, *Nature* **462**, 628 (2009).

[2] Y.-J. Lin, R. L. Compton, K. Jimenez-Garcia, W. D. Phillips,

- J. V. Porto, and I. B. Spielman, *Nat. Phys.* **7**, 531 (2011).
- [3] Y.-J. Lin, K. Jiménez-García, and I. B. Spielman, *Nature (London)* **471**, 83 (2011).
- [4] V. Galitski and I. B. Spielman, *Nature* **494**, 49 (2013).
- [5] N. Goldman, G. Juzeliūnas, P. Öhberg, and I. B. Spielman, *Reports on Progress in Physics* **77**, 126401 (2014).
- [6] J.-Y. Zhang, S.-C. Ji, Z. Chen, L. Zhang, Z.-D. Du, B. Yan, G.-S. Pan, B. Zhao, Y.-J. Deng, H. Zhai, S. Chen, and J.-W. Pan, *Phys. Rev. Lett.* **109**, 115301 (2012).
- [7] D. Campbell, R. Price, A. Putra, A. Valdés-Curiel, D. Trypogergos, and I. Spielman, *Nat. Commun.* **7**, 1 (2016).
- [8] X. Luo, L. Wu, J. Chen, Q. Guan, K. Gao, Z.-F. Xu, L. You, and R. Wang, *Sci. Rep.* **6**, 1 (2016).
- [9] L. W. Cheuk, A. T. Sommer, Z. Hadzibabic, T. Yefsah, W. S. Bakr, and M. W. Zwierlein, *Phys. Rev. Lett.* **109**, 095302 (2012).
- [10] P. Wang, Z.-Q. Yu, Z. Fu, J. Miao, L. Huang, S. Chai, H. Zhai, and J. Zhang, *Phys. Rev. Lett.* **109**, 095301 (2012).
- [11] R. A. Williams, M. C. Beeler, L. J. LeBlanc, K. Jiménez-García, and I. B. Spielman, *Phys. Rev. Lett.* **111**, 095301 (2013).
- [12] J.-R. Li, J. Lee, W. Huang, S. Burchesky, B. Shteynas, F. Ç. Top, A. O. Jamison, and W. Ketterle, *Nature* **543**, 91 (2017).
- [13] A. Putra, F. Salces-Cárcocha, Y. Yue, S. Sugawa, and I. B. Spielman, *Phys. Rev. Lett.* **124**, 053605 (2020).
- [14] C. Wang, C. Gao, C.-M. Jian, and H. Zhai, *Phys. Rev. Lett.* **105**, 160403 (2010).
- [15] T.-L. Ho and S. Zhang, *Phys. Rev. Lett.* **107**, 150403 (2011).
- [16] Y. Li, G. I. Martone, L. P. Pitaevskii, and S. Stringari, *Phys. Rev. Lett.* **110**, 235302 (2013).
- [17] G. I. Martone, F. V. Pepe, P. Facchi, S. Pascazio, and S. Stringari, *Phys. Rev. Lett.* **117**, 125301 (2016).
- [18] M. A. Khamehchi, Y. Zhang, C. Hamner, T. Busch, and P. Engels, *Phys. Rev. A* **90**, 063624 (2014).
- [19] S.-C. Ji, L. Zhang, X.-T. Xu, Z. Wu, Y. Deng, S. Chen, and J.-W. Pan, *Phys. Rev. Lett.* **114**, 105301 (2015).
- [20] Z.-Q. Yu, *Phys. Rev. A* **93**, 033648 (2016).
- [21] K. Sun, C. Qu, Y. Xu, Y. Zhang, and C. Zhang, *Phys. Rev. A* **93**, 023615 (2016).
- [22] L. Chen, H. Pu, Z.-Q. Yu, and Y. Zhang, *Phys. Rev. A* **95**, 033616 (2017).
- [23] K. T. Geier, G. I. Martone, P. Hauke, and S. Stringari, *Phys. Rev. Lett.* **127**, 115301 (2021); K. T. Geier, G. I. Martone, P. Hauke, W. Ketterle, and S. Stringari, *Phys. Rev. Lett.* **130**, 156001 (2023).
- [24] Rajat, Ritu, A. Roy, and S. Gautam, *Phys. Rev. A* **109**, 033319 (2024).
- [25] Rajat, P. Banger, and S. Gautam, [arXiv:2410.22178](https://arxiv.org/abs/2410.22178) (2024).
- [26] M. DeMarco and H. Pu, *Phys. Rev. A* **91**, 033630 (2015).
- [27] C. Qu, K. Sun, and C. Zhang, *Phys. Rev. A* **91**, 053630 (2015).
- [28] Y.-X. Hu, C. Miniatura, and B. Grémaud, *Phys. Rev. A* **92**, 033615 (2015).
- [29] K. Sun, C. Qu, and C. Zhang, *Phys. Rev. A* **91**, 063627 (2015).
- [30] L. Chen, H. Pu, and Y. Zhang, *Phys. Rev. A* **93**, 013629 (2016).
- [31] I. Vasić and A. Balaž, *Phys. Rev. A* **94**, 033627 (2016).
- [32] J. Hou, X.-W. Luo, K. Sun, and C. Zhang, *Phys. Rev. A* **96**, 011603 (2017).
- [33] D. Zhang, T. Gao, P. Zou, L. Kong, R. Li, X. Shen, X.-L. Chen, S.-G. Peng, M. Zhan, H. Pu, and K. Jiang, *Phys. Rev. Lett.* **122**, 110402 (2019).
- [34] H.-R. Chen, K.-Y. Lin, P.-K. Chen, N.-C. Chiu, J.-B. Wang, C.-A. Chen, P. Huang, S.-K. Yip, Y. Kawaguchi, and Y.-J. Lin, *Phys. Rev. Lett.* **121**, 113204 (2018).
- [35] P.-K. Chen, L.-R. Liu, M.-J. Tsai, N.-C. Chiu, Y. Kawaguchi, S.-K. Yip, M.-S. Chang, and Y.-J. Lin, *Phys. Rev. Lett.* **121**, 250401 (2018).
- [36] L. R. Liu, S. C. Wu, T. W. Liu, H. Y. Hsu, T. K. Shen, S. K. Yip, Y. Kawaguchi, and Y. J. Lin, [arXiv:2403.17403](https://arxiv.org/abs/2403.17403) (2024).
- [37] Y. Duan, Y. M. Bidasyuk, and A. Surzhykov, *Phys. Rev. A* **102**, 063328 (2020).
- [38] X.-L. Chen, S.-G. Peng, P. Zou, X.-J. Liu, and H. Hu, *Phys. Rev. Res.* **2**, 033152 (2020).
- [39] N. Chiu, Y. Kawaguchi, S. Yip, and Y. Lin, *New J. Phys.* **22**, 093017 (2020).
- [40] K.-J. Chen, F. Wu, J. Hu, and L. He, *Phys. Rev. A* **102**, 013316 (2020).
- [41] Y. M. Bidasyuk, K. S. Kovtunencko, and O. O. Prykhodko, *Phys. Rev. A* **105**, 023320 (2022).
- [42] P. Banger, Rajat, A. Roy, and S. Gautam, *Phys. Rev. A* **108**, 043310 (2023); P. Banger, Ph.D. thesis, Indian Institute of Technology Ropar (2024).
- [43] X.-L. Chen, A. Chen, and S.-G. Peng, *Phys. Rev. Res.* **6**, 033200 (2024).
- [44] A. Chaika, A. Richaud, and A. Yakimenko, *Phys. Rev. Res.* **5**, 023109 (2023).
- [45] O. O. Prykhodko and L. V. Zadorozhna, [arXiv:2411.01590](https://arxiv.org/abs/2411.01590) (2024).
- [46] S.-G. Peng, K. Jiang, X.-L. Chen, K.-J. Chen, P. Zou, and L. He, *AAPPS Bulletin* **32**, 36 (2022).
- [47] A. Crubellier, O. Dulieu, F. Masnou-Seeuws, M. Elbs, H. Knöckel, and E. Tiemann, *Eur. Phys. J. D* **6**, 211 (1999).
- [48] P. Kaur, A. Roy, and S. Gautam, *Comput. Phys. Commun.* **259**, 107671 (2021); P. Banger, P. Kaur, A. Roy, and S. Gautam, *Comput. Phys. Commun.* **279**, 108442 (2022); P. Banger, P. Kaur, and S. Gautam, *Int. J. Mod. Phys. C* **33**, 2250046 (2021); R. Ravisankar, D. Vudragović, P. Muruganandam, A. Balaž, and S. K. Adhikari, *Comput. Phys. Commun.* **259**, 107657 (2021).
- [49] Rajat, A. Roy, and S. Gautam, *Phys. Rev. A* **106**, 013304 (2022).
- [50] M.-O. Mewes, M. R. Andrews, N. J. van Druten, D. M. Kurn, D. S. Durfee, C. G. Townsend, and W. Ketterle, *Phys. Rev. Lett.* **77**, 988 (1996).
- [51] T. Bienaimé, E. Fava, G. Colzi, C. Mordini, S. Serafini, C. Qu, S. Stringari, G. Lamporesi, and G. Ferrari, *Phys. Rev. A* **94**, 063652 (2016).
- [52] A. Roy, S. Pal, S. Gautam, D. Angom, and P. Muruganandam, *Comput. Phys. Commun.* **256**, 107288 (2020).
- [53] R. B. Lehoucq, D. C. Sorensen, and C. Yang, *ARPACK Users' Guide* (Society for Industrial and Applied Mathematics, 1998) <https://epubs.siam.org/doi/pdf/10.1137/1.9780898719628>.
- [54] <https://www.netlib.org/lapack/>.